

Silicon substrate-integrated hollow waveguide for miniaturized optical gas sensing

SHAONAN ZHENG, HONG CAI, LINFANG XU, NANXI LI,*  ZHONGHUA GU, YAO ZHANG, WEIGUO CHEN, YANYAN ZHOU, QINGXIN ZHANG, AND LENNON YAO TING LEE

*Institute of Microelectronics, A*STAR (Agency for Science, Technology and Research), Singapore 138634, Singapore*

*Corresponding author: linx1@ime.a-star.edu.sg

Received 4 August 2021; revised 6 October 2021; accepted 7 November 2021; posted 11 November 2021 (Doc. ID 439434); published 24 December 2021

Gas sensors have a wide variety of applications. Among various existing gas sensing technologies, optical gas sensors have outstanding advantages. The development of the Internet of Things and consumer electronics has put stringent requirements on miniaturized gas sensing technology. Here, we demonstrate a chip-scale silicon substrate-integrated hollow waveguide (Si-iHWG) to serve as an optical channel and gas cell in an optical gas sensor. It is fabricated through silicon wafer etching and wafer bonding. The Si-iHWG chip is further assembled with an off-chip light source and detector to build a fully functional compact nondispersive infrared (NDIR) CO₂ sensor. The chip size is 10 mm × 9 mm, and the dimension of the sensor excluding the microcontroller board is 50 mm × 25 mm × 16 mm. This chip solution with compactness, versatility, robustness, and low cost provides a cost-effective platform for miniaturized optical sensing applications ranging from air quality monitoring to consumer electronics. © 2021 Chinese Laser Press

<https://doi.org/10.1364/PRJ.439434>

1. INTRODUCTION

Gas sensors have drawn significant interest from academic research to commercial applications [1–6]. Among various existing gas sensing technologies [7–15], optical gas sensors based on the interaction between photons and chemical gas molecules stand out for their high sensitivity, high selectivity, long life time, short response time, and long-term operation stability [16–20]. Many important gases have characteristic absorption lines in the mid-infrared (MIR) range (2–12 μm) [21], allowing high-selectivity and high-sensitivity detection. Hence, MIR sensors are highly desirable for increasing needs in various application scenarios. A conventional hollow waveguide (HWG) is widely used in transmitting IR light in a wide spectral range from 0.9 to 25 μm with low loss (0.5–1.5 dB/m at 10.6 μm) thanks to a dielectric layer as the inner coating of the metallic waveguide surface [22,23]. Various gas sensing and spectroscopic applications have been demonstrated exploiting an HWG with tens of centimeters to several meters coupled to spectrometer or laser to enable high sensitivity (down to ppb-level detection limit) [24–28]. However, conventional HWG is unsuitable for compact gas sensor due to its high cost and susceptibility to mechanical vibration and shock. Substrate-integrated HWGs (iHWGs) are emerging as a promising technology recently for gas sensing and spectroscopy [29,30]. They are fabricated into a mechanically robust substrate with small footprint to dramatically release the influence

of mechanical vibration and shock. In Ref. [29], a 21.8 cm long spiral iHWG with average loss of 2.32 dB/mm is developed and tested on an optical alignment system for sensing of several gases using a Fourier transform infrared (FTIR) spectrometer and HgCdTe (MCT) detector. A low limit of detection (LOD) of 21 ppm (parts per million) is achieved for CO₂ sensing. A fiber-coupled spiral iHWG (13.8 cm in length) is later experimentally tested using similar optical setup for gas sensing by the same research group in Ref. [30]. The calculated LODs are 34 ppm, 43 ppm, and 42 ppm for methane, isobutylene, and cyclopropane, respectively. However, iHWG built into a metal substrate requires expensive milling and polishing processes to realize submillimeter dimensions and smooth surface. A cost-effective way of iHWG fabrication is to leverage silicon wafer etching and bonding technology. A 2D cylinder shape optical/gas cell (4 mm diameter) fabricated on a silicon substrate by deep reactive ion etching (DRIE) is developed and experimentally tested on a fiber alignment system through fiber coupling, achieving an LOD of 100 ppm for CO₂ sensing [31]. Also, a hollow-core waveguide formed by two parallel silicon-on-insulator wafers has been reported with low optical loss of 0.37 dB/cm at 1535 nm [32]. Furthermore, solid-core waveguide sensing through an evanescent wave is widely recognized thanks to its high level of integration and low propagation and bending loss [33–38]. In Ref. [36], a 2 cm long silicon waveguide on Si₃N₄ membrane is tested on a fiber alignment system

where an external laser at the wavelength of $4.23\ \mu\text{m}$ is used for CO_2 sensing. The experimentally tested propagation loss is $3.98\ \text{dB/cm}$ at $4.17\ \mu\text{m}$ wavelength and the LOD is $500\ \text{ppm}$.

In comparison with solid-core waveguides, iHWG suffers from higher optical loss due to larger surface roughness and sensitivity to bending, hindering its applications, which requires ultralow detection limit (sub-ppm level). However, solid-core waveguide sensing in the MIR range is limited by its alignment tolerance with the light source and detector, which is due to the waveguide dimensions (hundreds of nanometers to a few micrometers). In the meanwhile, iHWG with much larger waveguide dimensions (a few hundred micrometers) allows direct free-space light coupling and significantly larger alignment tolerance with the light source and detector. Hence, the iHWG is viable for a chemical gas sensor working in the MIR wavelength range for applications requiring ppm-level detection limit.

To address the increasing needs of compact and low-cost gas sensors [4,21], in this work, the iHWGs fabricated into silicon wafer substrate are developed and experimentally demonstrated for chemical gas sensing. The demonstrated compact iHWGs are fabricated on an 8-inch (200 mm) standard silicon wafer for chemical gas sensing. By leveraging silicon wafer-scale etching and bonding processes, the Si-iHWG sensors can be mass-produced. Hence, the cost can be dramatically reduced compared with the iHWGs built into a metal substrate. Further, we experimentally demonstrated a fully functional compact nondispersive infrared (NDIR) CO_2 sensor by assembling the Si-iHWG chip with an off-chip source and detector. The Si-iHWG chip has a compact size of $10\ \text{mm} \times 9\ \text{mm}$, and the dimensions of the sensor excluding the microcontroller board are $50\ \text{mm} \times 25\ \text{mm} \times 16\ \text{mm}$. Promising application scenarios of the Si-iHWG based gas sensor include environmental monitoring and consumer electronics. Compared with the preliminary results presented in a conference [39], this work includes more details on Si-iHWG design and fabrication. Also, more discussions and analysis are included for waveguide loss and coupling loss measurement results, as well as gas sensing test results.

2. DESIGN AND WORKING PRINCIPLE

The schematic of a spiral iHWG formed on silicon wafer substrate (bottom wafer) is shown in Fig. 1(a). The Si-iHWG in an optical gas sensing system acts as both the optical waveguide and gas cell. The spiral path is designed to realize larger path length for higher sensitivity while maintaining a small footprint. The physical length of the spiral Si-iHWG is $34.07\ \text{mm}$. The bending radius is $2.2\ \text{mm}$. Figure 1(b) shows the schematic of the cross section. The designed semicircle radius is $250\ \mu\text{m}$. It is formed with one flat-top wafer and one etched-bottom wafer. The inner surfaces of both wafer substrates are coated with a reflective metallic film. Here, gold film is chosen as the reflective metallic film. In this work, the Si-iHWG chip is assembled with the off-chip light-emitting diode (LED, AKM AK9700AE) and photodetector (PD, AKM AK9710AEF01) by a specially designed holder to build an NDIR CO_2 sensor. The schematic assembly of LED, Si-iHWG, and PD is shown in Fig. 1(c). The LED has an emission area of $0.7\ \text{mm} \times 0.7\ \text{mm}$ and peak emission at the wavelength of $4.3\ \mu\text{m}$ with

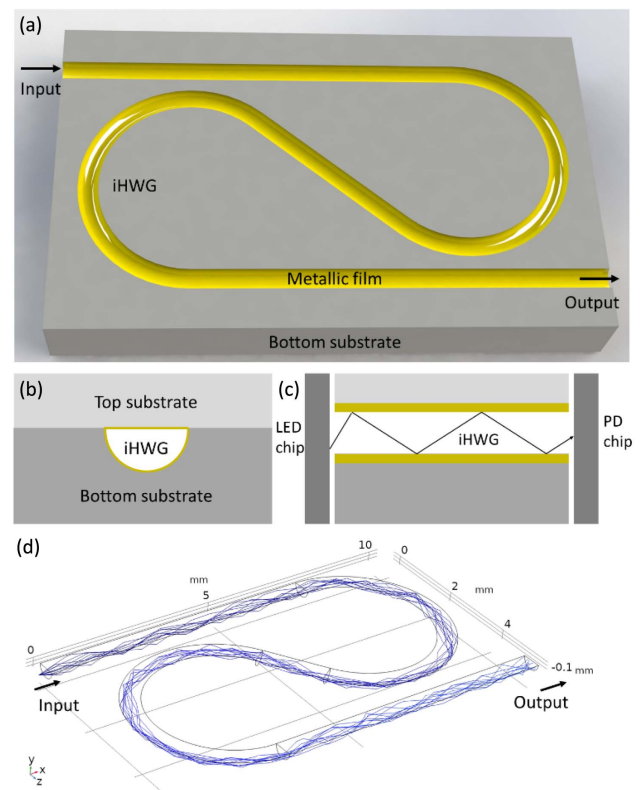


Fig. 1. (a) Schematic of a spiral iHWG etched on a silicon wafer substrate. (b) Cross section of the spiral iHWG. (c) Schematic assembly of LED, Si-iHWG, and PD. Drawings in (a)–(c) are not to scale. (d) Ray trajectory simulation in the spiral Si-iHWG. The source rays are the rays at 15° (angle between light ray and the x axis) and an axial ray in the x direction from a point emitter.

$1\ \mu\text{m}$ full width at half-maximum (FWHM), and the angle of half intensity is $\pm 30^\circ$. The LED and PD (denoted as PD_s) are placed closely (not in contact) at the input and output ports of the Si-iHWG. The PD_s has a sensitive detection area of $0.69\ \text{mm} \times 0.69\ \text{mm}$. The PD_s also has a built-in optical bandpass filter. Its center wavelength is $4.28\ \mu\text{m}$ and the FWHM is $270\ \text{nm}$. The light from LED is coupled into and out of the Si-iHWG to PD_s through free space. Light coupled into the Si-iHWG will interact with the gas of interest inside the Si-iHWG path and be detected by PD_s. In the LED chip, a reference PD (denoted as PD_{ref}) is placed closely to the LED emission area to detect part of the reflected light emitted from the LED [40]. During the light reflection process toward PD_{ref}, the path is sealed and does not interact with any gases. Hence, the signal from PD_{ref} serves as the reference signal here.

Based on Beer–Lambert law, with a monochromatic light source, the transmittance is expressed as

$$T = \frac{I}{I_0} = e^{-c\epsilon L}, \quad (1)$$

where I_0 is the initial light intensity at the input, I is the intensity at output after transmitting through the gas cell where light and the gas of interest interact, ϵ is the molar attenuation coefficient of the gas of interest, c is the gas concentration, and

L is the interaction length. Hence, for a target gas and a fixed length L , the gas concentration can be inferred by measuring the transmittance T . The transmittance can be obtained by normalizing the signal of PD_s with CO₂ absorption U_s to the baseline signal of PD_s without CO₂ absorption U_{s0} , i.e., with pure N₂. In the meantime, in actual deployment, the transmittance T for our NDIR CO₂ sensor using an off-chip LED and PD will need to be expressed as

$$T = k \frac{U_s}{U_r}, \quad (2)$$

where U_s is output voltage of PD_s and U_r is output voltage of PD_{ref}. U_r is used instead of U_{s0} , since in actual sensor deployment, we would not be flushing the sensor with pure N₂. Considering the two paths are different and the signal amplifications set in control circuits are different for the two PDs, a correction factor k is added. Therefore, we can obtain the following equation:

$$t = \frac{U_s}{U_r} = \frac{T}{k} = \frac{1}{k} e^{-cL}, \quad (3)$$

where t stands for the measured sensor response, which is proportional to transmittance T . One can see that the relation between sensor response t and CO₂ concentration c is exponential. Therefore, based on Eq. (3), through proper calibration between t and c to obtain their relation, we can infer CO₂ concentration by measuring the sensor response t .

Figure 1(d) shows the ray trajectory simulation in the spiral Si-iHWG. The source rays are the ones at 15° (angle between the light ray and x axis) and an axial ray in the x direction from a point emitter. In addition to the axial ray, only the rays at 15° are chosen to represent the overall rays in order to clearly visualize the ray trajectory within the Si-iHWG. The Si-iHWG works as a leaky guide. Light propagates inside through reflection by gold film coated at the inner surfaces. Si-iHWG can transmit light from coherent and incoherent sources, depending on target applications. For instance, a coherent source such as laser source has high power at sensing wavelength to allow for higher sensitivity applications.

3. EXPERIMENTAL SECTION

A. Fabrication of Si-iHWG

Figure 2 shows the fabrication process of Si-iHWG with a semicircular cross section. The drawing is not to scale. It starts with two 8-inch (200 mm) silicon wafers, one as the bottom wafer for Si-iHWG formation and the other as the top covering wafer to form the top part of the Si-iHWG. For the bottom wafer, a dense gold film is firstly deposited as a hard mask through the sputtering process, which is wet etched later using potassium iodide solution. The silicon substrate is thereafter wet etched to obtain a smooth semicircular cross-sectional shape. Afterwards, the gold hard mask is removed, and a 300 nm thick gold film is deposited uniformly as the reflection layer through evaporation. Gold film is chosen due to its high reflectivity (99.5%) near wavelength of 4 μm [41] and suitability for wafer bonding. The top wafer is firstly etched by DRIE followed by silicon isotropic etching to form funnel-shaped blind holes. Then back grinding is performed to form

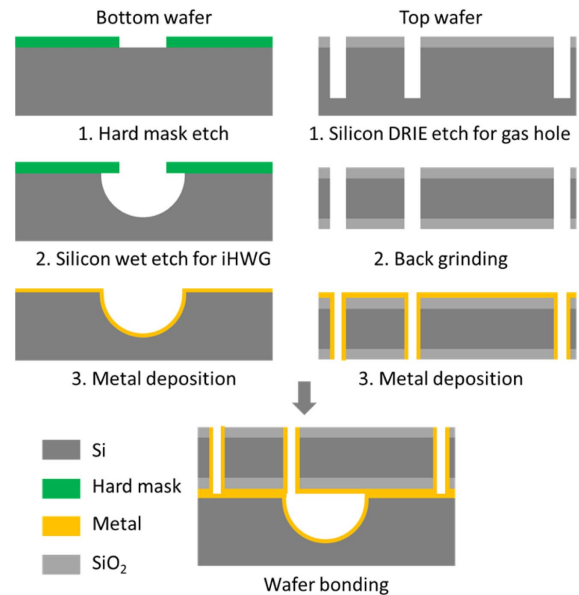


Fig. 2. Fabrication process of Si-iHWG with a semicircular cross section. Drawing is not to scale. Two silicon wafers are used, one as the bottom wafer for Si-iHWG formation and the other as the top covering wafer to form the top part of the Si-iHWG. The top wafer and the bottom wafer are bonded together to form the Si-iHWG.

funnel-shaped through holes. Thereafter, another 300 nm thick gold film is deposited uniformly on the surface as the reflection layer through evaporation. Such gold film deposition is done as the last step in order to avoid any particle contamination that could impact the inner surface reflection. The thin wafer after back-grinding is handled by temporarily hosting it on a supporting silicon wafer for further process. Finally, the 8-inch (200 mm) top wafer and the bottom wafer are bonded together at 300°C with 3 kN force for 2.5 h to form the Si-iHWG.

Figure 3(a) shows the optical micrograph of a Si-iHWG chip consisting of a straight Si-iHWG and a spiral Si-iHWG. The physical lengths of the straight and spiral Si-iHWGs are 10 mm and 34.07 mm, respectively. The chip footprint is 10 mm × 9 mm. The dashed curves denote the path of the Si-iHWGs. Gas holes are fabricated in top wafer to allow gas diffusion. Figure 3(b) shows the scanning electron microscopy (SEM) image of a Si-iHWG cross section after silicon wet etching on the bottom wafer substrate, where the measured top width is 589 μm and the maximum etch depth is 271 μm. The etch depth deviation is due to wafer fabrication nonuniformity during silicon substrate wet etching. Figure 3(c) shows the SEM image of part of a spiral Si-iHWG after silicon wet etching on the bottom wafer substrate. The SEM image of the Si-iHWG cross section after wafer bonding is illustrated in Fig. 3(d). Gas holes are on the edges of Si-iHWG to minimize optical loss induced by gas holes and allow enough gas exchange at the same time. The atomic force microscopy (AFM) measurement on etched silicon blanket test wafer (without gold film) shows a surface roughness root-mean-square (RMS) value between 1.3 and 3.3 nm, which is at comparable level with the AFM measurement on a reference raw silicon wafer surface without any fabrication. The surface will induce propagation

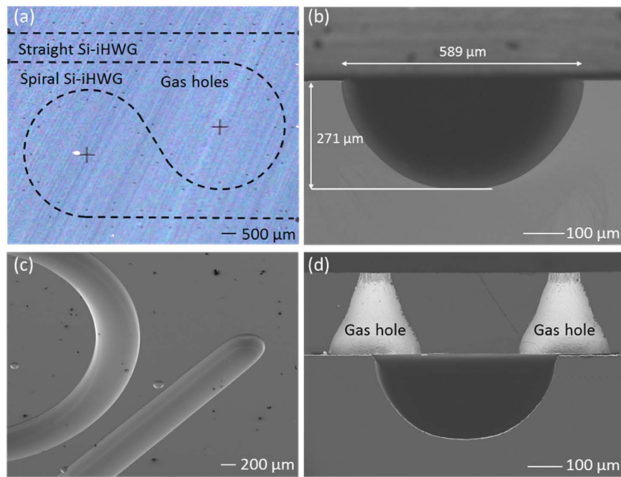


Fig. 3. (a) Optical micrograph of a Si-iHWG chip consisting of a straight Si-iHWG and a spiral Si-iHWG. The chip footprint is 10 mm × 9 mm. (b) SEM image of the Si-iHWG cross section after silicon wet etching on the bottom wafer substrate. (c) SEM image of a spiral Si-iHWG after silicon wet etching on the bottom wafer substrate. (d) SEM image of the Si-iHWG cross section after wafer bonding.

loss due to scattering. Hence, low surface roughness is desirable to reduce propagation loss to improve sensor sensitivity.

B. Si-iHWG Loss Characterization Setup

Figure 4 shows the schematic of experimental setup for Si-iHWG loss characterization. The Si-iHWG chip is mounted on a six-axis optical fiber alignment system for characterization. The loss measurement is conducted in a normal laboratory environment. A tunable laser (M Squared Firefly IR) is used as the light source. The laser tuning range is from 3294 to 4277 nm. The linewidth is $<6 \text{ cm}^{-1}$. Two 2 m ZBLAN multimode fluoride fibers from FiberLabs (ZMF-160/200-N-0.29) are used to couple light into and out of the Si-iHWGs. The source is coupled from free space to the input fiber using a focusing lens. A HgCdTe photodetector (Thorlabs PDAVJ10) is used to measure the output power from the output fiber. Manual alignment between the optical fibers and Si-iHWG is performed to find the maximal output power.

C. Sensor Testing Setup

A fully functional NDIR CO₂ sensor is built by assembling a Si-iHWG chip with off-chip LED and PD. Figure 5(a) shows the NDIR CO₂ sensor prototype. The holder is used to assemble the Si-iHWG chip, LED, and PD. The LED and PD have

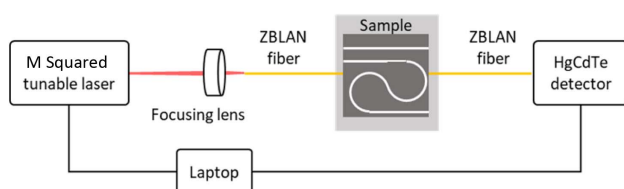


Fig. 4. Experimental setup for Si-iHWG loss characterization. ZBLAN: ZrF₄-BaF₂-LaF₃-AlF₃-NaF. A sample chip is placed at a six-axis optical fiber alignment system for loss characterization. A laptop is used for laser control and data acquisition from the detector.

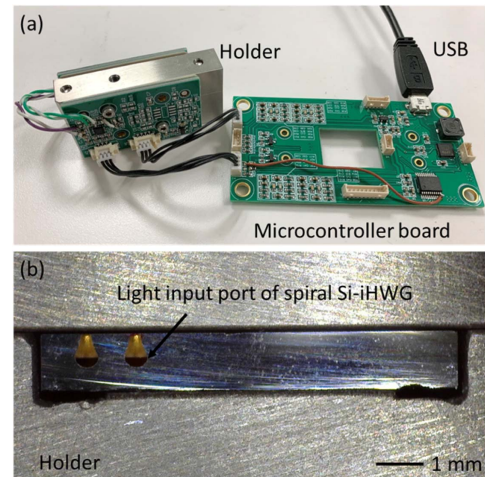


Fig. 5. (a) Fully functional NDIR CO₂ sensor prototype by assembling a Si-iHWG chip with off-chip LED and PD. (b) Side view of the Si-iHWG chip fixed by the holder.

surface mount packages and are mounted on two sides of the Si-iHWG chip. The dimension of the assembled sensor excluding microcontroller board is 50 mm × 25 mm × 16 mm. The form factor of the Si-iHWG sensor can be further reduced by adopting a more compact assembly method. Figure 5(b) shows the side view of the Si-iHWG chip fixed by the holder. The input ports of the straight and spiral Si-iHWGs can be seen clearly. The 34.07 mm long spiral Si-iHWG is used in the sensor. Once the assembly is completed, the mechanical holder itself can provide optical alignment with enough precision. Hence, no further active optical alignment is needed.

Figure 6 shows the schematic of experimental setup for CO₂ gas testing. The whole assembled sensor shown in Fig. 5 together with the microcontroller board is placed inside a gas chamber. The gas chamber is in cylindrical shape with a diameter of 170 mm and a height of 60 mm. The body is made of aluminum with non-conductive coatings on inner surfaces, and the cap is made of acrylate. The gas flow is controlled by mass flow controllers (Bronkhorst MFC, F-201CV). The chamber has gas inlet and outlet connectors for connection with the gas tubes of MFCs and exhaust, respectively. The gas chamber allows gas exchange and prevents gas leakage. To achieve various CO₂ concentrations, we mix CO₂ with N₂ from two certified gas cylinders (5000 ppm CO₂ and 99.9999% N₂, respectively), and we precisely and independently control the

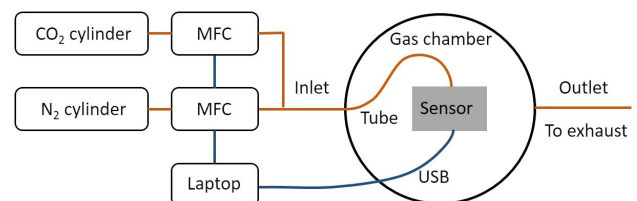


Fig. 6. Gas testing setup. Gas flows from two cylinders are precisely and independently controlled by two mass flow controllers (MFCs). The gas flow rate into sensor inlet is fixed at 500 standard cubic centimeters per minute (SCCM).

two mass flow controllers (MFCs). The gas flow rate into the sensor inlet is fixed at 500 standard cubic centimeters per minute (SCCM). After mixed gas is guided into the chamber from the MFC, it is subsequently guided by another tube directly into the inlet of the sensor and diffused into the spiral Si-iHWG through gas holes fabricated on the top substrate. Since the full gas exchange of the whole chamber takes 15 min, the tube is used here to direct the mixed gas quickly to the sensor for reduction of the sensor response time. There is no obvious difference in sensor response signal observed except that the response time is reduced significantly if the tube is used. This response time mainly depends on the gas exchange rate. The gas measurements are also conducted in a normal laboratory environment. The USB cable connects the sensor microcontroller board to a laptop for power supply and data acquisition.

4. RESULTS AND DISCUSSIONS

A. Si-iHWG Loss Analysis

Figures 7(a) and 7(b) show the measured propagation loss and coupling loss of the straight Si-iHWG, respectively, in the 35 nm spectral range. Five chips chosen across the same wafer

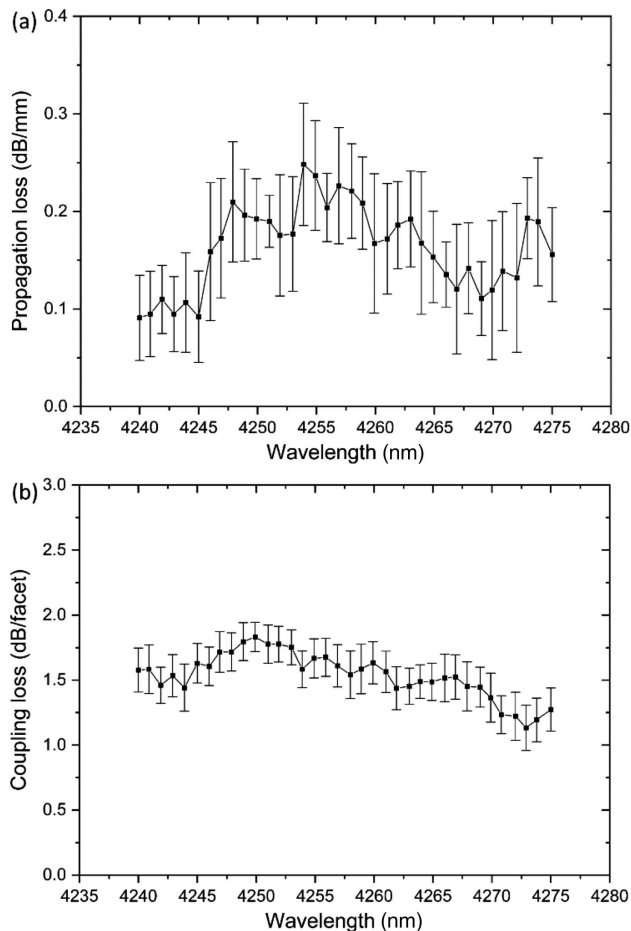


Fig. 7. (a) Propagation loss of straight Si-iHWG. (b) Coupling loss between optical fiber and straight Si-iHWG. The error bars in (a) and (b) denote standard deviations of propagation loss from repeated measurements and coupling loss measured from the waveguides with five different lengths, respectively.

are measured. Each chip consists of a straight Si-iHWG with a different length. The waveguide lengths of 2.5, 4, 5, 5.5, and 7 mm are used for waveguide loss and coupling loss measurement. Due to cross-sectional dimension variations of Si-iHWGs across the whole wafer and variations contributed by manual alignment, the average propagation loss and average coupling loss are extracted and shown as data points in Fig. 7. Please note that the error bars in Figs. 7(a) and 7(b) denote standard deviations of propagation loss from repeated measurements and coupling loss measured from the waveguides with five different lengths, respectively. From the experimental data, propagation loss in the straight Si-iHWG is 0.17 ± 0.07 dB/mm and coupling loss is 1.63 ± 0.16 dB/facet at the wavelength of 4260 nm. The measured straight waveguide loss and coupling loss with variations can be explained as follows. Firstly, the nonperfect inner surface will induce propagation losses due to scattering and nonperfect reflections of light during transmission. Since the loss experiment is conducted in the open air of a normal laboratory, light will be attenuated due to absorption of atmospheric CO_2 . Hence, lower waveguide propagation loss is expected. Also, from the simulation of ray tracing, light rays with larger divergence angle tend to encounter more reflections and hence experience higher propagation loss. Secondly, light coupling between Si-iHWG and optical fiber will induce coupling loss due to dimension mismatch between optical fiber and Si-iHWG. In a non-straight Si-iHWG, bending will also induce additional loss, since a hollow waveguide is inherently sensitive to bending and the total loss depends strongly on the bending radius. Light will experience a larger number of reflections to transmit through a bending with smaller radius, resulting in larger bending loss. This loss can be reduced by coiling the Si-iHWG with a larger radius, which in turn will increase the footprint. An additional note worth mentioning is that the Si-iHWG waveguide is expected to have broad optical bandwidth in MIR wavelength regime since Au has high reflectivity ($>99.5\%$) within such wavelength regime [41]. The measured loss variation at different wavelengths in Fig. 7 should be mainly contributed by the experimental setup, including the coupling loss variation at different wavelengths and laser power instability during the testing.

To measure the insertion loss, seven identical chips chosen from the same wafer as shown in Fig. 3(a) are tested. The total insertion loss of a straight Si-iHWG (10 mm) and a spiral Si-iHWG (34.07 mm) is measured to be 4.68 ± 0.49 dB and 7.23 ± 0.33 dB at 4260 nm wavelength, respectively. Due to fabrication variations between different wafers, the loss values vary among different wafers. By comparing with straight Si-iHWG, the loss due to bending (2.2 mm bending radius) in the spiral Si-iHWG is not significant. The reason is that the coiling radius is large enough. Furthermore, to reduce the loss of the iHWG in the future, the reflective metal (Au) deposition process can be further optimized to make the metal surface smoother. Also, the waveguide etching process can be optimized to get better surface smoothness, and post-thermal treatment can be applied to smooth surface spikes.

B. Gas Sensing Analysis

Figure 8(a) shows the detected power, i.e., U_s and U_r , from PD_s and PD_{ref}, respectively, under different CO_2

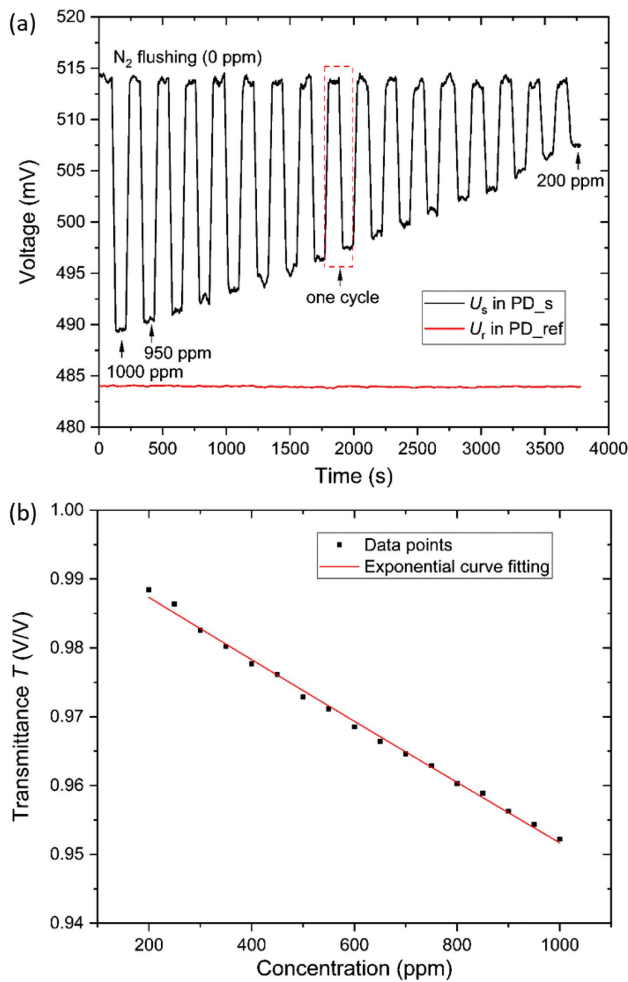


Fig. 8. (a) Output voltage from PD_s and PD_{ref} while changing CO₂ concentration of mixed gas. The CO₂ concentration is changed from 1000 ppm to 200 ppm at a concentration step of 50 ppm. N₂ purging is performed every time before changing the CO₂ concentration. (b) Relation between transmittance T and CO₂ concentration. The data points are obtained by normalizing average value of U_s with CO₂ presence to baseline signal, i.e., average value of $U_{s,0}$ with N₂ purging in each cycle.

concentrations of mixed gas. A 30 s moving average has been applied in the sensor control circuit to improve signal-to-noise ratio. The CO₂ concentration is changed from 1000 ppm to 200 ppm in sequence at a CO₂ concentration step of 50 ppm. It is worth mentioning that the CO₂ concentration range in this test is based on the gas concentration available experimentally, to demonstrate the gas sensing functionality implementing the iHWG. N₂ purging is performed every time before changing the CO₂ concentration. The injection of pure N₂ followed by mixed gas is called one cycle as highlighted by a box with a red-dotted line in Fig. 8(a). The duration of N₂ purging is 2 min, and the duration of one cycle is 4 min. The transmittance T in Fig. 8(b) is obtained by normalizing the average value of U_s with CO₂ presence to baseline signal, i.e., average value of $U_{s,0}$ with N₂ purging in each cycle. Figure 8(b) shows the experimental data T well fitted to CO₂ concentration with

an exponential curve. One can see the relation matches well with the Beer–Lambert law expressed as Eq. (1).

Figure 9(a) shows the sensor response t while changing the CO₂ concentration of mixed gas. The sensor response t is calculated from the voltage values in Fig. 8(a) using $t = U_s/U_r$, as provided in Eq. (3). Please note that the black curves in Figs. 8(a) and 9(a) look similar since U_r does not have significant change over time, which can be seen in the red curve of Fig. 8(a). Figure 9(b) shows the relation between sensor response t and CO₂ concentration extracted from Fig. 9(a). The data points are the average values of sensor response t in each cycle. The error bars denote the standard deviations of sensor response t in each cycle. The experimental average value of sensor response t is well fitted to CO₂ concentration with an exponential curve $t = ae^{-bc}$ and a good fitting $R^2 = 0.9969$, which agrees well with the relation expressed in Eq. (3). The fitting parameters are $a = 1.06$ and $b = 5 \times 10^{-5}$. Gas testing results show the Si-iHWG sensor can be used to detect CO₂ concentration ranging from 200 ppm to 1000 ppm.

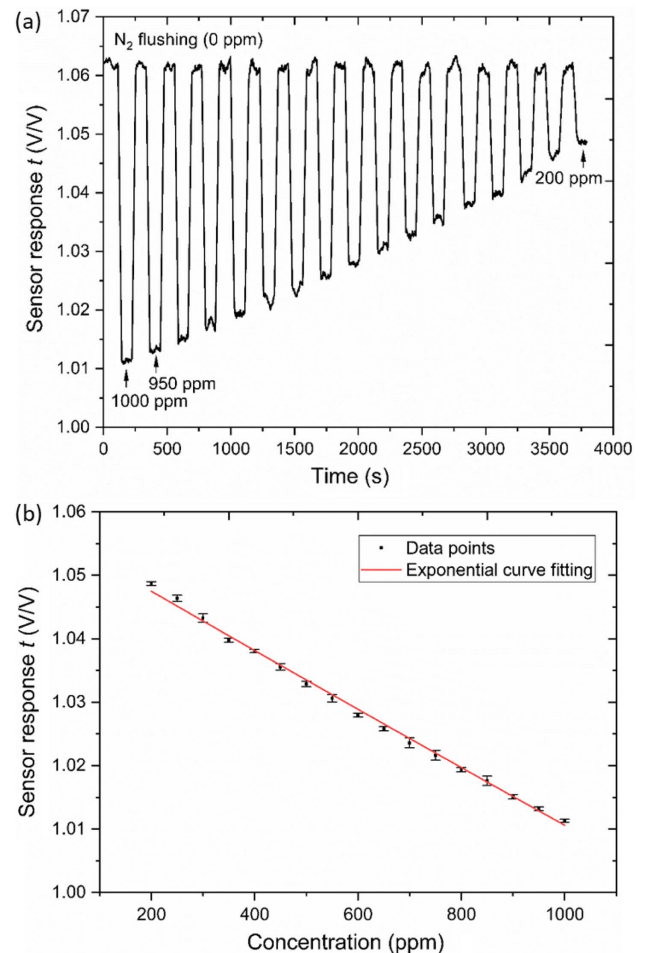


Fig. 9. (a) Sensor response t while changing CO₂ concentration of mixed gas. (b) Relation between sensor response t and CO₂ concentration. The data points are the average values of sensor response t in each cycle. The error bars denote the standard deviations of sensor response t in each cycle.

5. CONCLUSION

In conclusion, Si-iHWGs are demonstrated for miniaturized gas sensing. The reported Si-iHWGs are formed by wet etching silicon wafer and wafer bonding. The chip footprint consisting of a straight and a spiral Si-iHWGs is 10 mm × 9 mm. Propagation loss in the straight Si-iHWG is 0.17 ± 0.07 dB/mm, and coupling loss is 1.63 ± 0.16 dB/facet at 4260 nm wavelength. A fully functional NDIR sensor for CO₂ detection is further experimentally demonstrated by assembling a spiral Si-iHWG with off-chip LED and PD. The optical path of the Si-iHWG can be configured to different geometries such as straight, spiral, and serpentine to adapt to a wide range of path lengths and locations of light input and output ports. The footprint is limited mainly by the bending loss and can be reduced further by using a smaller bending radius. The designed 34.07 mm spiral Si-iHWG length is mainly limited by the die size and waveguide bending loss. In addition to path length tailorability, Si-iHWGs are compatible with coherent and incoherent sources. Also, they are compatible with free space and fiber coupling for light input and output. Hence, they are suitable for various applications. Furthermore, Si-iHWG is transparent in the MIR range due to broadband nature of hollow waveguides to enable sensing of many important gases, e.g., CH₄, CO, and NO. Wafer-based Si-iHWGs enable mass production and compatibility with integrated light sources and detectors [42–49] to realize a fully integrated sensor, which would be even more compact and with lower cost. This will require advanced packaging technology to bond source and detector onto the Si-iHWG chip.

Funding. Agency for Science, Technology and Research (IAF-PP A1789a0024, IAF-PP A19B3a0008); Robert Bosch (SEA) Pte. Ltd.

Acknowledgment. The authors thank Dr. Doris Keh Ting Ng for discussions. Also, the authors appreciate the fruitful discussions with experts from Robert Bosch (SEA) Pte. Ltd.

Disclosures. The authors declare no conflicts of interest.

Data Availability. Data underlying the results presented in this paper are not publicly available at this time but may be obtained from the authors upon reasonable request.

REFERENCES

1. R. A. Potyrailo, "Multivariable sensors for ubiquitous monitoring of gases in the era of internet of things and industrial internet," *Chem. Rev.* **116**, 11877–11923 (2016).
2. H. Yuan, N. Li, J. Linghu, J. Dong, Y. Wang, A. Karmakar, J. Yuan, M. Li, P. J. S. Buenconsejo, G. Liu, H. Cai, S. J. Pennycook, N. Singh, and D. Zhao, "Chip-level integration of covalent organic frameworks for trace benzene sensing," *ACS Sens.* **5**, 1474–1481 (2020).
3. S. Feng, F. Farha, Q. Li, Y. Wan, Y. Xu, T. Zhang, and H. Ning, "Review on smart gas sensing technology," *Sensors* **19**, 3760 (2019).
4. L. Sari, Y. Rafic, A. Yasser, and S. Mohamad, "Review of recent trends in gas sensing technologies and their miniaturization potential," *Sens. Rev.* **34**, 24–35 (2014).
5. N. Liu, M. L. Tang, M. Hentschel, H. Giessen, and A. P. Alivisatos, "Nanoantenna-enhanced gas sensing in a single tailored nanofocus," *Nat. Mater.* **10**, 631–636 (2011).
6. H. Yuan, G. Liu, Z. Qiao, N. Li, P. J. S. Buenconsejo, S. Xi, A. Karmakar, M. Li, H. Cai, S. J. Pennycook, and D. Zhao, "Solution-processable metal–organic framework nanosheets with variable functionalities," *Adv. Mater.* **33**, 2101257 (2021).
7. B. Chocarro-Ruiz, J. Pérez-Carvajal, C. Avci, O. Calvo-Lozano, M. I. Alonso, D. MasPOCH, and L. M. Lechuga, "A CO₂ optical sensor based on self-assembled metal–organic framework nanoparticles," *J. Mater. Chem. A* **6**, 13171–13177 (2018).
8. J. Wu, M. Yin, K. Seefeldt, A. Dani, R. Guterman, J. Yuan, A. P. Zhang, and H.-Y. Tam, "In situ μ -printed optical fiber-tip CO₂ sensor using a photocrosslinkable poly(ionic liquid)," *Sens. Actuators B Chem.* **259**, 833–839 (2018).
9. H. Yuan, J. Tao, N. Li, A. Karmakar, C. Tang, H. Cai, S. J. Pennycook, N. Singh, and D. Zhao, "On-chip tailorability of capacitive gas sensors integrated with metal–organic framework films," *Angew. Chem.* **58**, 14089–14094 (2019).
10. M. R. Tchalala, Y. Belmabkhout, K. Adil, K. N. Chappanda, A. Cadiou, P. M. Bhatt, K. N. Salama, and M. Eddaoudi, "Concurrent sensing of CO₂ and H₂O from air using ultramicroporous fluorinated metal–organic frameworks: effect of transduction mechanism on the sensing performance," *ACS Appl. Mater. Interface* **11**, 1706–1712 (2019).
11. H. Yuan, J. Cui, N. Li, M. Li, X. Yu, W. Fan, A. Karmakar, J. Dong, S. J. Pennycook, H. Cai, and D. Zhao, "On-chip template-directed conversion of metal hydroxides to metal–organic framework films with enhanced adhesion," *ACS Appl. Mater. Interface* **12**, 36715–36722 (2020).
12. C. Sun, Q. Shi, D. Hasan, M. S. Yazici, M. Zhu, Y. Ma, B. Dong, Y. Liu, and C. Lee, "Self-powered multifunctional monitoring system using hybrid integrated triboelectric nanogenerators and piezoelectric microsensors," *Nano Energy* **58**, 612–623 (2019).
13. F. Juang, "Ag additive and nanorod structure enhanced gas sensing properties of metal oxide-based CO₂ sensor," *IEEE Sens. J.* **19**, 4381–4385 (2019).
14. S. Kanaparthi and S. G. Singh, "Chemiresistive sensor based on zinc oxide nanoflakes for CO₂ detection," *ACS Appl. Nano Mater.* **2**, 700–706 (2019).
15. N. B. Tanvir, O. Yurchenko, E. Laubender, R. Pohle, O. V. Sicard, and G. Urban, "Zinc peroxide combustion promoter in preparation of CuO layers for conductometric CO₂ sensing," *Sens. Actuators B Chem.* **257**, 1027–1034 (2018).
16. X. Liu, S. Cheng, H. Liu, S. Hu, D. Zhang, and H. Ning, "A survey on gas sensing technology," *Sensors* **12**, 9635–9665 (2012).
17. J. Hodgkinson and R. P. Tatam, "Optical gas sensing: a review," *Meas. Sci. Technol.* **24**, 012004 (2012).
18. B. Robert, "Detecting gases with light: a review of optical gas sensor technologies," *Sens. Rev.* **35**, 133–140 (2015).
19. T.-V. Dinh, I.-Y. Choi, Y.-S. Son, and J.-C. Kim, "A review on non-dispersive infrared gas sensors: improvement of sensor detection limit and interference correction," *Sens. Actuators B Chem.* **231**, 529–538 (2016).
20. N. Li, H. Yuan, L. Xu, Y. Zeng, B. Qiang, Q. J. Wang, S. Zheng, H. Cai, L. Y. T. Lee, N. Singh, and D. Zhao, "Tailorable infrared emission of microelectromechanical system-based thermal emitters with NiO films for gas sensing," *Opt. Express* **29**, 19084–19093 (2021).
21. D. Popa and F. Udreă, "Towards integrated mid-infrared gas sensors," *Sensors* **19**, 2076 (2019).
22. C. M. Charlton, B. T. Thompson, and B. Mizaikoff, "Hollow waveguide infrared spectroscopy and sensing," in *Frontiers in Chemical Sensors: Novel Principles and Techniques*, G. Orellana and M. C. Moreno-Bondi, eds. (Springer, 2005), pp. 133–167.
23. P. Patimisco, V. Spagnolo, M. S. Vitiello, G. Scamarcio, C. M. Bledt, and J. A. Harrington, "Low-loss hollow waveguide fibers for mid-infrared quantum cascade laser sensing applications," *Sensors* **13**, 1329–1340 (2013).
24. S.-S. Kim, N. Menegazzo, C. Young, J. Chan, C. Carter, and B. Mizaikoff, "Mid-infrared trace gas analysis with single-pass Fourier transform infrared hollow waveguide gas sensors," *Appl. Spectrosc.* **63**, 331–337 (2009).
25. X. Li, J. Pawlat, J. Liang, and T. Ueda, "Measurement of low gas concentrations using photonic bandgap fiber cell," *IEEE Sens. J.* **10**, 1156–1161 (2010).

26. N. Liu, J. Sun, H. Deng, J. Ding, L. Zhang, and J. Li, "Recent progress on gas sensor based on quantum cascade lasers and hollow fiber waveguides," *Proc. SPIE* **10250**, 102501W (2017).
27. T. Wu, W. Kong, M. Wang, Q. Wu, W. Chen, C. Ye, R. Hu, and X. He, "Compact hollow waveguide mid-infrared gas sensor for simultaneous measurements of ambient CO₂ and water vapor," *J. Lightwave Technol.* **38**, 4580–4587 (2020).
28. J. Li, G. Luo, Z. Du, and Y. Ma, "Hollow waveguide enhanced dimethyl sulfide sensor based on a 3.3 μm interband cascade laser," *Sens. Actuators B Chem.* **255**, 3550–3557 (2018).
29. A. Wilk, J. C. Carter, M. Chrisp, A. M. Manuel, P. Mirkarimi, J. B. Alameda, and B. Mizaikoff, "Substrate-integrated hollow waveguides: a new level of integration in mid-infrared gas sensing," *Anal. Chem.* **85**, 11205–11210 (2013).
30. E. Tütüncü, V. Kokoric, A. Wilk, F. Seichter, M. Schmid, W. E. Hunt, A. M. Manuel, P. Mirkarimi, J. B. Alameda, J. C. Carter, and B. Mizaikoff, "Fiber-coupled substrate-integrated hollow waveguides: an innovative approach to mid-infrared remote gas sensors," *ACS Sens.* **2**, 1287–1293 (2017).
31. X. Jia, J. Roels, R. Baets, and G. Roelkens, "On-chip non-dispersive infrared CO₂ sensor based on an integrating cylinder," *Sensors* **19**, 4260 (2019).
32. W. Yang, J. Ferrara, K. Grutter, A. Yeh, C. Chase, Y. Yue, A. E. Willner, M. C. Wu, and C. J. Chang-Hasnain, "Low loss hollow-core waveguide on a silicon substrate," *Nanophotonics* **1**, 23–29 (2012).
33. L. Tombez, E. J. Zhang, J. S. Orcutt, S. Kamlapurkar, and W. M. J. Green, "Methane absorption spectroscopy on a silicon photonic chip," *Optica* **4**, 1322–1325 (2017).
34. E. J. Zhang, Y. Martin, J. S. Orcutt, C. Xiong, M. Glodde, N. Marchack, E. A. Duch, T. Barwicz, L. Schares, and W. M. Green, "Monolithically integrated silicon photonic chip sensor for near-infrared trace-gas spectroscopy," *Proc. SPIE* **11010**, 110100B (2019).
35. C. Ranacher, C. Consani, A. Tortschanoff, R. Jannesari, M. Bergmeister, T. Grille, and B. Jakoby, "Mid-infrared absorption gas sensing using a silicon strip waveguide," *Sens. Actuators A Phys.* **277**, 117–123 (2018).
36. C. Ranacher, C. Consani, N. Vollert, A. Tortschanoff, M. Bergmeister, T. Grille, and B. Jakoby, "Characterization of evanescent field gas sensor structures based on silicon photonics," *IEEE Photon. J.* **10**, 2700614 (2018).
37. P. Su, Z. Han, D. Kita, P. Becla, H. Lin, S. Deckoff-Jones, K. Richardson, L. C. Kimerling, J. Hu, and A. Agarwal, "Monolithic on-chip mid-IR methane gas sensor with waveguide-integrated detector," *Appl. Phys. Lett.* **114**, 051103 (2019).
38. F. Ottonello-Briano, C. Errando-Herranz, H. Rödjegård, H. Martin, H. Sohlström, and K. B. Gylfason, "Carbon dioxide absorption spectroscopy with a mid-infrared silicon photonic waveguide," *Opt. Lett.* **45**, 109–112 (2020).
39. S. Zheng, H. Cai, L. Xu, N. Li, J. Fu, Z. Gu, Y. Zhang, W. Chen, Y. Cui, and F. M. Kai, "Miniaturized gas sensor based on silicon substrate-integrated hollow waveguides," *Proc. SPIE* **11689**, 116890C (2021).
40. E. G. Camargo and S. Takehara, "Gas sensor," U.S. patent 10,551,314 (4 February 2020).
41. S. Babar and J. H. Weaver, "Optical constants of Cu, Ag, and Au revisited," *Appl. Opt.* **54**, 477–481 (2015).
42. N. Li, H. Yuan, L. Xu, J. Tao, D. K. T. Ng, L. Y. T. Lee, D. D. Cheam, Y. Zeng, B. Qiang, Q. Wang, H. Cai, N. Singh, and D. Zhao, "Radiation enhancement by graphene oxide on microelectromechanical system emitters for highly selective gas sensing," *ACS Sens.* **4**, 2746–2753 (2019).
43. D. Jung, S. Bank, M. L. Lee, and D. Wasserman, "Next-generation mid-infrared sources," *J. Opt.* **19**, 123001 (2017).
44. S. Z. Ali, A. De Luca, R. Hopper, S. Boual, J. Gardner, and F. Udrea, "A low-power, low-cost infra-red emitter in CMOS technology," *IEEE Sens. J.* **15**, 6775–6782 (2015).
45. N. Li, Q. Chao, Z. Gu, S. Song, Y. Zhou, S. Zheng, L. Xu, Y. Da Chua, Q. Zhang, and H. Cai, "Photonic crystal MEMS emitter for chemical gas sensing," *Proc. SPIE* **11697**, 116970M (2021).
46. B. J. O'Regan, Y. Wang, and T. F. Krauss, "Silicon photonic crystal thermal emitter at near-infrared wavelengths," *Sci. Rep.* **5**, 13415 (2015).
47. J. Faist, F. Capasso, D. L. Sivco, C. Sirtori, A. L. Hutchinson, and A. Y. Cho, "Quantum cascade laser," *Science* **264**, 553–556 (1994).
48. N. Li, E. S. Magden, Z. Su, N. Singh, A. Ruocco, M. Xin, M. Byrd, P. T. Callahan, J. D. B. Bradley, C. Baiocco, D. Vermeulen, and M. R. Watts, "Broadband 2-μm emission on silicon chips: monolithically integrated holmium lasers," *Opt. Express* **26**, 2220–2230 (2018).
49. H. Lin, Z. Luo, T. Gu, L. C. Kimerling, K. Wada, A. Agarwal, and J. Hu, "Mid-infrared integrated photonics on silicon: a perspective," *Nanophotonics* **7**, 393–420 (2017).